Available online at www.sciencedirect.com

SciVerse ScienceDirect

Ceramics International 38 (2012) 2857–2863

CERAMICS INTERNATIONAL

www.elsevier.com/locate/ceramint

A study of the oxidation of ZrB_2 powders during high-energy ball-milling in air

Angel L. Ortiz *, Victor Zamora, Fernando Rodríguez-Rojas

Department of Mechanical, Energy, and Materials Engineering, University of Extremadura, 06006 Badajoz, Spain

Received 14 June 2011; received in revised form 7 November 2011; accepted 21 November 2011
Available online 28 November 2011

Abstract

Oxide impurities in ZrB_2 powders promote coarsening, resulting in lower sinterability. Given its importance for sintering, we studied the oxidation of ZrB_2 powders during high-energy ball-milling (the form of milling able to refine ZrB_2 powders to the nanoscale) with the aid of various characterization techniques, namely fusion in inert gas, X-ray diffractometry, helium pycnometry, transmission electron microscopy, and Fourier-transform infrared, Raman, and X-ray photoemission spectroscopy. It was found that high-energy ball-milling in air introduces twice as much oxygen into the ZrB_2 powders as the more conventional attrition milling. Also, this oxygen does not form solid-solutions with ZrB_2, but amorphous oxides (i.e., ZrO_2 and B_2O_3) that locate preferentially on the surface of the ultra-fine agglomerates resulting from cold-welding of the primary nano-particles that form during the ball-milling.

Keywords: ZrB_2; Ultra-high-temperature ceramics; High-energy ball-milling

1. Introduction

It has been demonstrated that the refinement of the starting powders and the elimination of surface oxide impurities are two key processing steps to enhance the solid-state sinterability of the poorly sinterable ZrB_2 powders that are being used to process ultra-high-temperature ceramics (UHTCs) [1–7]. The reduction in the particle size shortens the diffusion distance of the chemical species, thus speeding up the densification kinetics significantly for the interparticle-diffusion controlled sintering [8], something that is especially relevant in ZrB_2 due to the serious kinetic restrictions imposed by its strong covalent bonding and its low self-diffusion coefficients [9]. It is not surprising therefore that the typical micrometre-sized ZrB_2 particles need to be refined to the submicrometre range before the sintering heat-treatment. With respect to surface oxide impurities in non-oxide ceramics, they are known to favor the evaporation–condensation mass transport mechanism [10], and this promotes coarsening thus reducing the driving force for densification and limiting the final density [10]. Hence, it is necessary to remove the surface oxides of ZrO_2 and B_2O_3 in ZrB_2 at temperatures below which coarsening is significant (1650–1850 °C) to thus retain the original particle size up to the temperatures where densification can proceed.

In most studies on ZrB_2 UHTCs, the starting powders are refined by wet attrition milling using some alcohol or inert organic solvent as liquid media [3,4]. Under these wet operating conditions, attrition milling is actually conventional ball-milling because the liquid media reduces the milling intensity, so that its function is only comminution (i.e., particle size reduction). The typical ZrB_2 particles achieved by attrition milling have submicrometre sizes (between 0.6 and 0.2 μm), much smaller than the micrometre-sized particles (~2 μm) of the commonest commercially available ZrB_2 powders. The current practice used to remove the surface oxides of ZrO_2 consists of adding to the ZrB_2 powders sintering additives with the potential to act as reducing agents, the most widely used of which are C, B_4C, and WC [1,2,5,11]. The removal of B_2O_3 from the surface of ZrB_2 is by evaporation, simply maintaining an actively pumped vacuum at temperatures below 1650 °C [2,6]. Apart from the intrinsic surface oxide layer in the ZrB_2 particles, further oxidation of the ZrB_2 powder occurs during the attrition milling. Typically, between 1 and 2 wt.% oxygen is

* Corresponding author. Tel.: +34 924289600x86726; fax: +34 924289601.
E-mail addresses: alortiz@materiales.unex.es, alortiz@unex.es (A.L. Ortiz).

0272-8842/$36.00
doi:10.1016/j.ceramint.2011.11.058

introduced during attrition milling under flowing argon gas atmosphere, and a little bit more (i.e., ∼2 wt.%) if the milling is conducted in air [1–3,6,7,11–14].

Recently, it has been shown that high-energy ball-milling in dry conditions using shaker mills can refine the ZrB_2 powders to the nanoscale [15–17], something that conventional ball-milling cannot do. This is because the mechanism of crystal size refinement in ZrB_2 is brittle fracture, where the fracture strength scales inversely with the square root of the crystal size [18], and the compressive stresses generated during the high-energy ball-milling are high enough (i.e., GPa) to fracture fine particles [19,20]. This refinement to the nanoscale offers unprecedented opportunities to enhance sintering kinetics immensely, as has been demonstrated lately [21]. An aspect that has received no attention to date despite its importance is the oxidation of the ZrB_2 powders during high-energy ball-milling in air. Predicting this oxidation a priori is difficult because high-energy ball-milling times are fairly short (∼3 h) relative to attrition milling times (∼24 h), which contributes to minimizing the oxidation, whereas the milling intensity is much higher and the nano-particles are more air-sensitive, which factors have the opposite effect.

With these premises in mind, the present study was undertaken with the objective of investigating the oxidation of ZrB_2 powders induced by their high-energy ball-milling in air, because milling in air would simplify the routine of powder preparation. The study includes determination of the oxygen uptake, and the structural and chemical statuses of the captured oxygen.

2. Experimental procedure

The starting powder was a commercially available micrometre ZrB_2 powder with 99% purity and single-crystal particles of average size 2 μm. The as-purchased ZrB_2 powder was subjected to high-energy ball-milling using a shaker mill (Spex D8000, Spex CertiPrep, Metuchen, NJ, US) operated at about 1060 back-and-forth cycles per minute. The milling was carried out in a cylindrical hardened-steel container with WC balls (6.7 mm in diameter) at a ball-to-powder weight ratio of 4, for 180 min, in air. Subsequently, the ball-milled powder was analyzed using various characterization techniques: transmission electron microscopy (TEM) for the direct examination of the size and morphology of the powder particles and nanocrystals, inert gas fusion (IGF) for the determination of the oxygen uptake, X-ray diffractometry (XRD) for the identification of the amorphous or crystalline nature of the phases present, helium pycnometry for the measurement of the density, and Fourier-transform infrared (FTIR), Raman, and X-ray photoemission (XPS) spectroscopy for the determination of the bonding environment or status.

The TEM observations were made at 200 kV in bright-field mode, using two conventional microscopes (Tecnai G^2 20 Twin, FEI, Eindhoven, The Netherlands; and JEM-2100, JEOL, Croissy-sur-Seine, France). The oxygen content measurements were done with an IGF determinator (TC-136, Leco Instrument, St. Joseph, MI, US) using graphite crucibles, helium gas, and Ni as flux. The XRD data were collected in step-scanning mode (step width 0.02° 2θ, and count time 3 s/step) using a high-resolution laboratory diffractometer (D8 Advance, Bruker AXS, Karlsruhe, Germany) equipped with a primary monochromator that provides pure CuKα_1 radiation (λ = 1.54183 Å) and a linear ultra-fast detector. Two measurement ranges were employed: 20–80°, and 20–55°. The phases present were identified with the aid of the PDF2 database, and were quantified using the Rietveld method (Topas 4.1, Bruker AXS, Karlsruhe, Germany). The density measurements were made by helium pycnometry (Stereopycnometer, Quantachrome Instruments, Hartley Wintney, UK). The FTIR spectra were recorded in the 4000–400 cm^{-1} range on a conventional spectrophotometer (Nicolet iS10, Thermo Scientific, East Grinstead, UK), using the KBr pellet method and an accumulation condition of 60 scans at 1 cm^{-1} resolution. The Raman spectra were measured in the 1000–125 cm^{-1} range using a micro-Raman spectrometer (Nicolet Almega XR, Thermo Scientific) equipped with a 633 nm He–Ne laser operated at 5.25 mW power, and were the result of 10 accumulations lasting 1 s. The XPS spectra of the Zr 3d and B 1s core lines were recorded in ultra-high vacuum (10^{-6} Pa) in the 176–194 eV range at 0.4 eV energy resolution using a high-resolution spectrometer (K-Alpha, Thermo Scientific) equipped with a monochromatic Al-Kα X-ray source (1486.6 eV). The C 1s peak was used to correct the binding energies in the XPS spectra. The protocol of sample preparation for each of these techniques followed standard procedures for ceramic powders.

3. Results and discussion

Fig. 1 compares representative TEM images of the as-purchased ZrB_2 powder and of the ZrB_2 powder ball-milled for 180 min in air. Clearly, the high-energy ball-milling has reduced the particle size by one order of magnitude from the micrometre scale (∼2–3 μm) to the nanometre scale (∼120–200 nm). Furthermore, higher-magnification TEM images such as that shown in Fig. 2 indicate that the powder particles after high-energy ball-milling are actually porous agglomerates consisting of many individual tiny single-crystals with an average size of ∼10 nm.

The oxygen contents determined by IGF were 1.537 and 4.514 wt.% for the as-purchased and ball-milled ZrB_2 powders, respectively, so that one can conclude that there is an oxygen uptake of ∼3 wt.% during the high-energy ball-milling in air. This oxygen content is greater than those typically reported for ZrB_2 powders prepared by attrition milling which are normally in the 2–3 wt.% range depending on the exact milling conditions [1–3,6,7,11–14]. To explore the structural and chemical statuses of the oxygen captured during the high-energy ball-milling in air, an exhaustive characterization of the ball-milled powder was needed, as we shall describe next.

Fig. 3 compares the XRD patterns of the ZrB_2 powder before and after the high-energy ball-milling for 180 min in air. Apart from the reduction in the peak intensity, the marked peak broadening, and the increase in the background after the high-energy ball-milling that together reflect the crystallite size

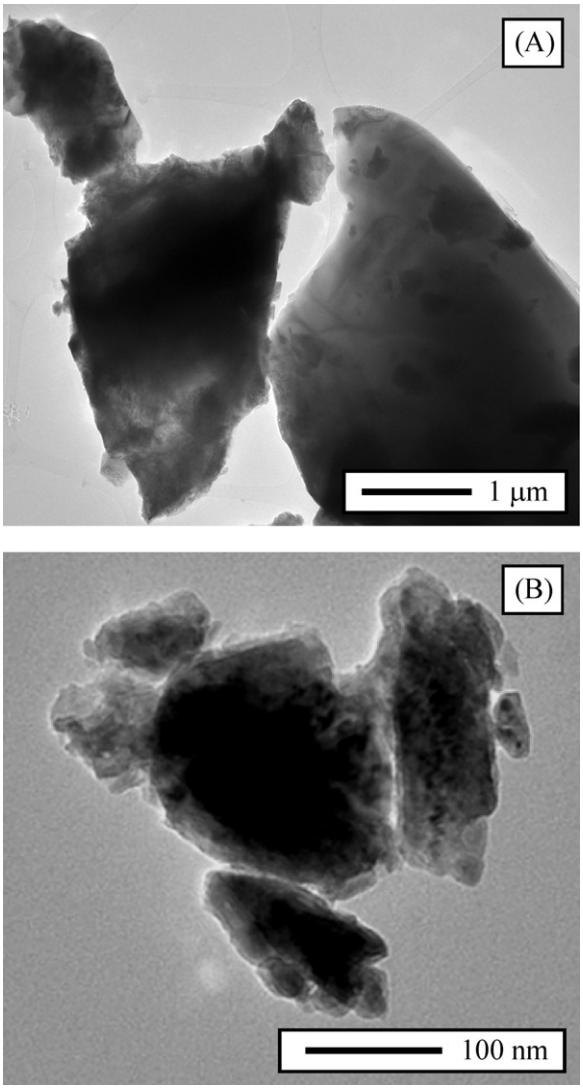

Fig. 1. TEM bright-field images of the ZrB_2 powder particles (a) in the as-purchased condition, and (b) after high-energy ball-milling for 180 min in air.

refinement to the nanoscale (~10 nm), and the presence of additional peaks that reveal the introduction of 2.5 wt% of WC according to the corresponding Rietveld analysis, there are another two important features in the figure. The first is that the ZrB_2 peaks remain in place. Since the absence of peak shifting excludes the formation of solid-solutions with oxygen atoms as solutes in the ZrB_2 host, it can be concluded that the oxygen captured during the high-energy ball-milling in air has formed oxides. The second is the absence of ZrO_2 and/or B_2O_3 peaks in the XRD patterns of the ball-milled ZrB_2 powder. Taking this observation together with the previous one, one can conclude that these oxides are amorphous. One could nevertheless argue that it would be very difficult to detect B_2O_3 by XRD in the presence of ZrB_2 because the scattering factor of Zr will dominate the entire diffractogram. Nevertheless, ZrO_2 should be detected which would prove the oxidation via the reaction $ZrB_2 + 5/2\ O_2(g) \rightarrow ZrO_2 + B_2O_3$ if this oxidation reaction had resulted in crystalline oxides. It could also be argued that crystalline ZrO_2 and B_2O_3 are formed during the high-energy

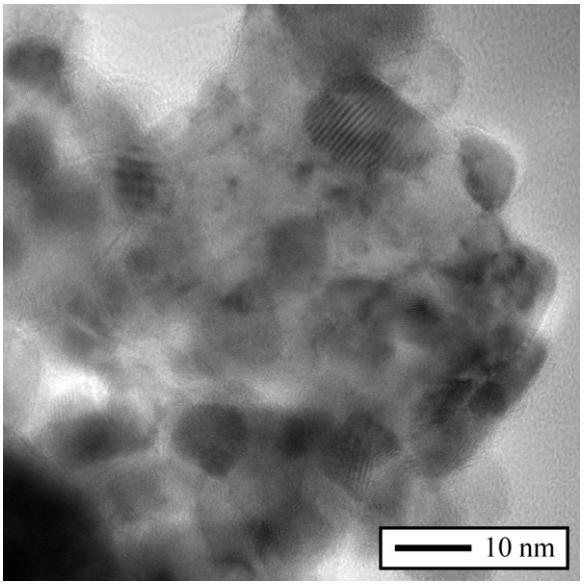

Fig. 2. TEM bright-field image of the interior of the ZrB_2 powder particles with 180 min of high-energy ball-milling in air, showing the agglomeration and cold-welding of individual primary nano-particles with 10 nm size.

ball-milling in air, but at amounts below the XRD detection limit. However, given the oxygen content determined by IGF and assuming equimolar formation of ZrO_2 and B_2O_3 as predicted by the above reaction, their concentrations is estimated to be 6.95 and 3.93 wt.%, respectively, which are clearly high enough to be detected by XRD. To prove that this is indeed the case, two powder mixtures in which 1 wt.% crystalline ZrO_2 was added to ZrB_2 were prepared and analyzed by XRD. In one of these two mixtures the crystals had submicrometre sizes and in the other nanometre sizes, done so as to rule out any crystallite-size effect in the detection of crystalline ZrO_2 in ZrB_2-based powders. It can be seen in Fig. 4

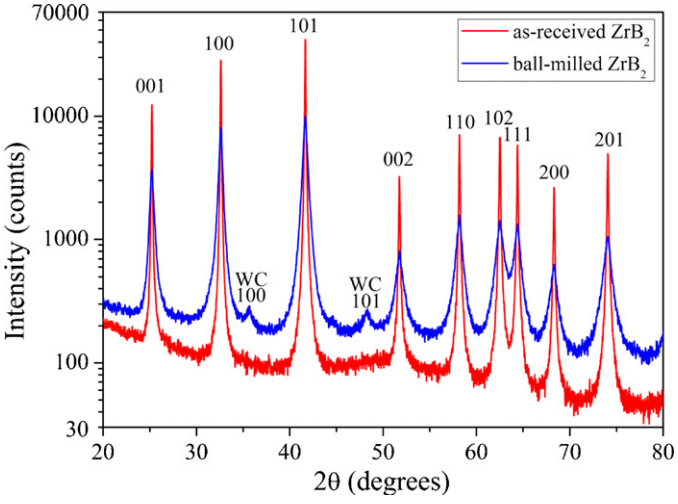

Fig. 3. XRD patterns of the ZrB_2 powders before and after high-energy ball-milling for 180 min in air. The WC peaks free of overlap with ZrB_2 peaks (which have been indexed) are marked. The logarithmic scale is to facilitate appreciation of the WC peaks (also indexed). (For interpretation of the references to color in the artwork, the reader is referred to the web version of the article.)

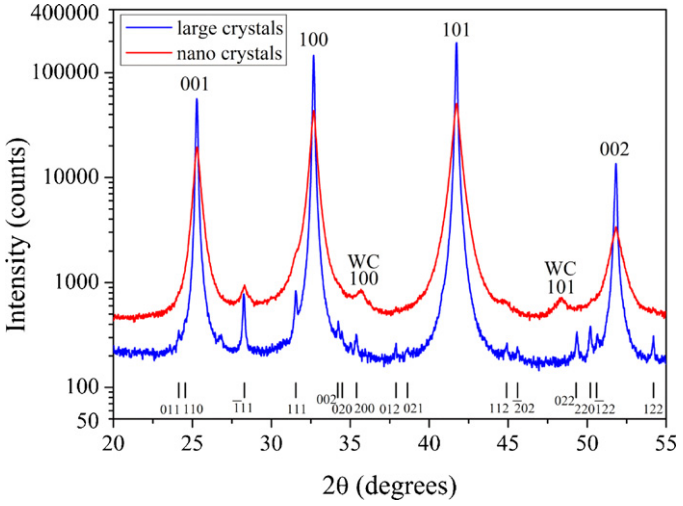

Fig. 4. XRD patterns of the ZrB_2 + 1 wt.% ZrO_2 powder mixtures with coarse crystals and with nano-crystals. The WC peaks free of overlap with ZrB_2 peaks (which have been indexed) are marked. The position of the ZrO_2 peaks is marked with short vertical lines. The logarithmic scale is to facilitate appreciation of the ZrO_2 and WC peaks (also indexed). (For interpretation of the references to color in the artwork, the reader is referred to the web version of the article.)

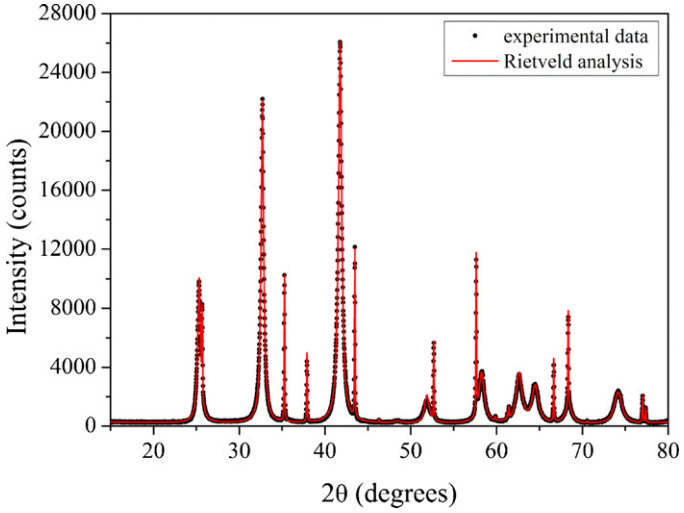

Fig. 5. Rietveld analysis of the XRD pattern of the ZrB_2 powder with 180 min of high-energy ball-milling in air plus 30 wt.% of Al_2O_3 powder. The points are the experimental data and the solid line is the Rietveld refinement.

that, despite the low ZrO_2 concentration of only 1 wt.%, the XRD patterns of these mixtures exhibit clear peaks of this oxide. Hence, these observations confirm that the oxide concentration deduced from IGF is above the detection limit of the diffractometer, and therefore that the oxides formed during high-energy ball-milling in air are amorphous because otherwise they would have been detected.

Despite its non-crystalline nature, the amorphous-phase content in the ball-milled ZrB_2 powder can be estimated from its XRD pattern using the Rietveld method in conjunction with the spiking technique (known crystallinity internal-standard method). In the present study, 30 wt.% Al_2O_3 was used as the spike phase because it provides a sufficient number of peaks in the XRD pattern with no overlap with the ZrB_2 peaks, and because its oxide nature rules out the presence of a passivating amorphous layer. With this XRD analysis, as shown in Fig. 5, the amorphous-phase content in the ball-milled ZrB_2 powder was calculated to be 12 wt.%, which is clearly consistent with the oxide concentration (i.e., ZrO_2 + B_2O_3) determined by IGF (∼11 wt.%).

The measurements of the powder density performed by helium pycnometry also lend strong credence to the formation of amorphous oxides, as they show that the density decreases from 6.12 g cm^{-3} in the as-purchased condition to 5.82 g cm^{-3} after 180 min of high-energy ball-milling in air. Using the rule-of-mixture with the values of theoretical density and volume concentrations determined experimentally of ZrB_2 (6.1 g cm^{-3}, 86.94 wt.%), WC (17.67 g cm^{-3}, 2.23 wt.%), ZrO_2 (5.86 g cm^{-3}, 6.91 wt.%) and B_2O_3 (2.46 g cm^{-3}, 3.93 wt.%), the density of the ball-milled powder was calculated to be 5.826 g cm^{-3}, in perfect agreement with the experimental measurement.

To further investigate the formation of amorphous ZrO_2 and B_2O_3 during the high-energy ball-milling of ZrB_2 in air, FTIR and Raman spectroscopy studies were conducted with the aim of detecting the vibration bands of the Zr–O and B–O bonds. Shown in Figs. 6 and 7 are, respectively, the FTIR and Raman spectra of the as-purchased and ball-milled ZrB_2 powders, together with the spectra of ZrO_2 and B_2O_3 powders that were also collected experimentally and included for comparison. As can be seen in Fig. 6, not only are the FTIR spectra from the two ZrB_2 powders similar, but neither do they exhibit the vibration bands typical of ZrO_2 and B_2O_3. As shown in Fig. 7, this scenario is also valid for the Raman spectra, despite ZrB_2 not being Raman active [22] which in principle should have facilitated the detection of the Raman peaks of ZrO_2 and B_2O_3.

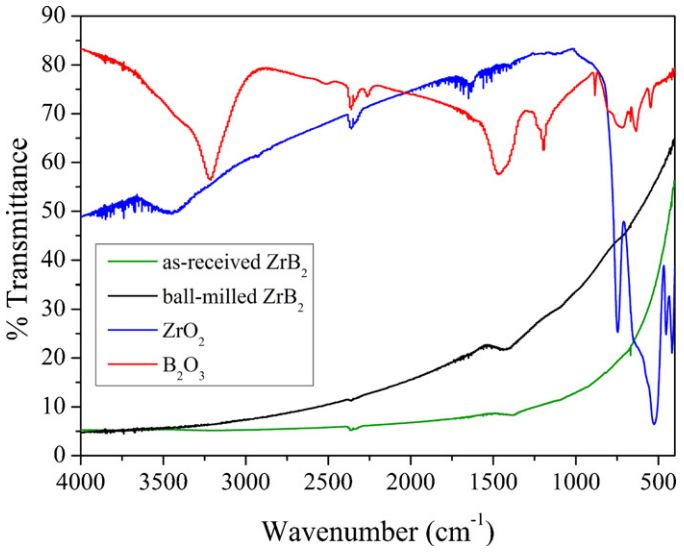

Fig. 6. FTIR spectra of the ZrB_2 powders before and after high-energy ball-milling for 180 min in air. The FTIR spectra of ZrO_2 and B_2O_3 have been included for comparison. The bands at ∼2350, 1400 and 670 cm^{-1} and the noise at 3900–3650 and 1830–1430 cm^{-1} are due to background. (For interpretation of the references to color in the artwork, the reader is referred to the web version of the article.)

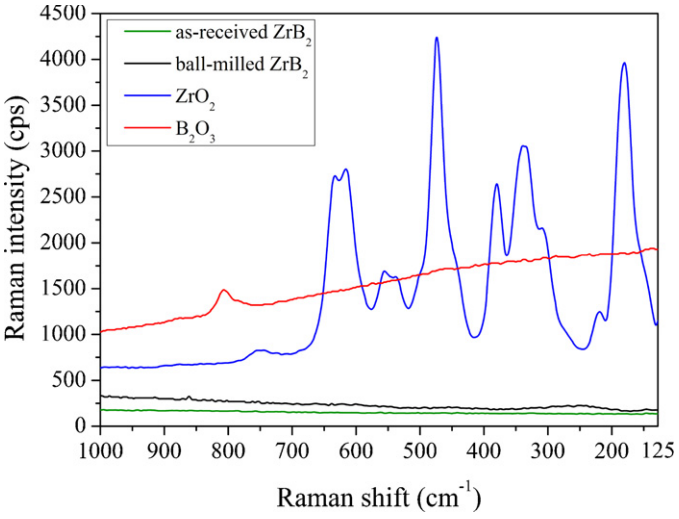

Fig. 7. Raman spectra of the ZrB_2 powders before and after high-energy ball-milling for 180 min in air. The Raman spectra of ZrO_2 and B_2O_3 have been included for comparison. (For interpretation of the references to color in the artwork, the reader is referred to the web version of the article.)

Thus, it can be concluded that the FTIR and Raman spectroscopic studies are unable to conclusively discriminate the presence of the concentrations of ZrO_2 and B_2O_3 formed during the high-energy ball-milling of ZrB_2 in air.

To confirm the formation of amorphous oxides as deduced from the XRD, IGF and helium pycnometry analyzes, the as-purchased and ball-milled ZrB_2 powders were investigated by XPS, which is a spectroscopic technique with a far better detection limit than FTIR or Raman spectroscopy. In particular, we monitored the binding energy of the Zr 3d and B 1s core levels before and after the high-energy ball-milling for 180 min in air (Fig. 8). One observes that the Zr 3d core level shows the typical $3d_{5/2}$ and $3d_{3/2}$ spin–orbit split, while the B 1s core level exhibits the typical single peak. However, two Zr $3d_{5/2}$–$3d_{3/2}$ doublets and two B 1s singlets are observed in each powder, which is a clear sign of the existence of two different bonding statuses for the Zr and B atoms. In both the as-purchased and the ball-milled powders, one set of Zr $3d_{5/2}$–$3d_{3/2}$ doublets plus B 1s singlet is located at binding energies of ~179.2, 181.6, and 188.2 eV, respectively, values which are due to ZrB_2 [23,24]. The other set of doublets plus singlet appears at higher binding energies of ~183.5, 185.9, and 193.1 eV, respectively, which are due to ZrO_2 and B_2O_3 [23,24]. One also observes that the ZrO_2/ZrB_2 and B_2O_3/ZrB_2 peak intensity ratios are greater in the powder subjected to high-energy ball-milling in air. Therefore, XPS has unambiguously detected the presence of ZrO_2 and B_2O_3 in the as-purchased and ball-milled ZrB_2 powders, and also shows them to be much more abundant in the ball-milled powder. Also noted in the XPS spectra of the two powders are that the ZrO_2 related peaks are more intense than the ZrB_2 related peaks. This observation, together with the oxygen contents that showed that the oxides are minor components and the fact that XPS is a surface technique, indicate that ZrO_2 and B_2O_3 cover the surface of the ZrB_2 particles. This hypothesis was further tested experimentally in the ball-milled powder by etching the surface with Ar^+ ions to remove material followed by XPS data collection, and also by TEM. One observes in Fig. 9 that the ZrB_2/ZrO_2 and ZrB_2/B_2O_3 peak intensity ratios increase after the etching, a clear sign that the ZrB_2 powder particles are covered by an oxide layer. As can be seen in Fig. 10, the direct high-resolution TEM observations also support the presence of an amorphous nano-film at the fringe of the agglomerates. This oxide distribution is attributed to two factors: (i) the lower chemical affinity between the oxides and ZrB_2 than between ZrB_2 crystals themselves which would promote cold-welding during the high-energy ball-milling via contacts of the type ZrB_2–ZrB_2; and (ii) the spontaneous surface passivation of ball-milled powder particles when exposed to ambient conditions after the high-energy ball-milling.

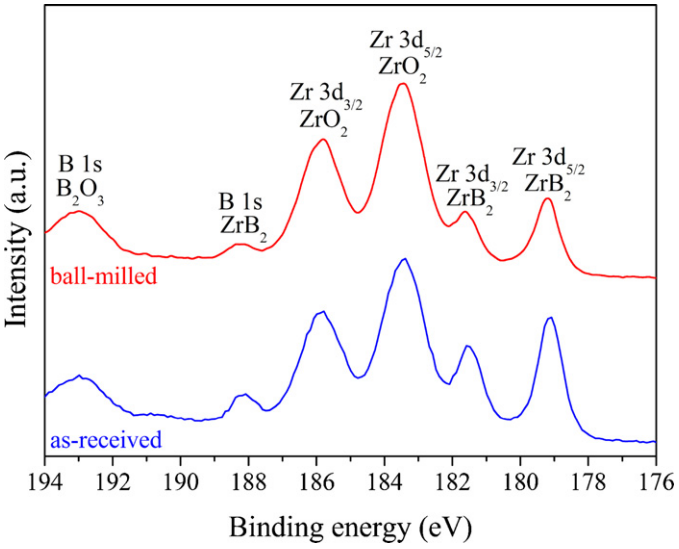

Fig. 8. High-resolution XPS spectra of the Zr 3d and B 1s core-levels for the ZrB_2 powders before and after high-energy ball-milling for 180 min in air. Also included in the figure is the peak indexing. The spectra have been shifted along the *Y*-axis to facilitate comparison.

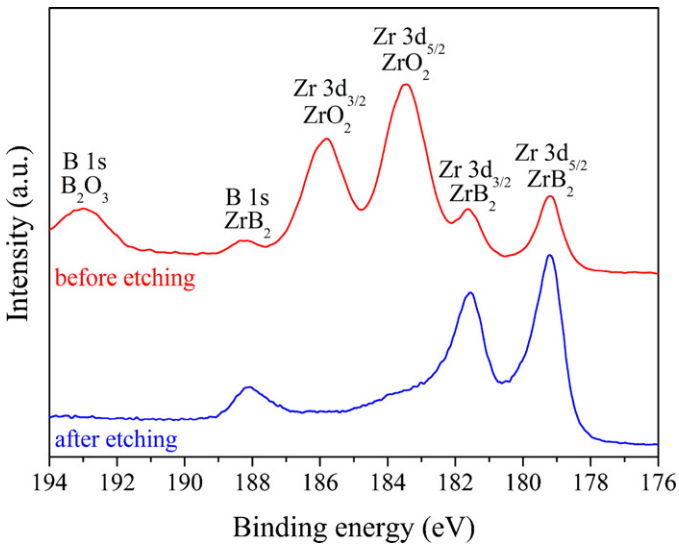

Fig. 9. High-resolution XPS spectra of the Zr 3d and B 1s core-levels for the ZrB_2 powders with 180 min of high-energy ball-milling in air before and after etching with Ar^+ ions. Also included in the figure is the peak indexing. The spectra have been shifted along the *Y*-axis to facilitate comparison.

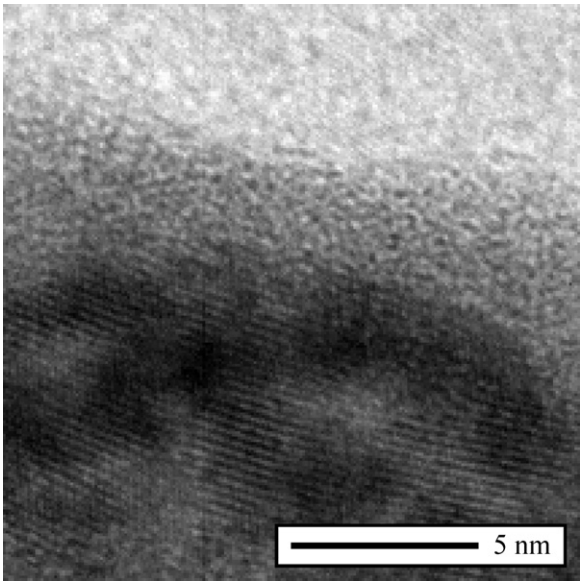

Fig. 10. High-resolution TEM bright-field image of the fringe of the ZrB_2 powder particles with 180 min of high-energy ball-milling in air, showing the presence of an amorphous region of nanometric thickness.

Finally, it is worth mentioning that a recent spark-plasma sintering (SPS) study [21] has revealed that the greater oxygen content of this ZrB_2 nano-powder obtained by high-energy ball-milling in air does not hinder its densification. On the contrary, it exhibits improved SPS kinetics relative to powders with larger particles and less oxygen content, which has been attributed to the large inter-particle boundary surface area[1] that can greatly enhance grain-boundary diffusion at lower temperatures. Whether the SPS results can or not be extrapolated to the pressureless sintering (PS) is something that has yet to be investigated experimentally. Whichever the case, it is reasonable to think that the sinterability of this ZrB_2 nano-powder (by SPS, PS, or hot-pressing) would improve further if the high-energy ball-milling were performed in an inert atmosphere, although the comminution routine would be more tedious and costly.

4. Concluding remarks

We have described an investigation of the oxidation of ZrB_2 powders during their high-energy ball-milling in air, using various analytical techniques. The direct measurement of the oxygen content by the IGF method revealed that the powders subjected to high-energy ball-milling in air are twice as rich in oxygen as those subjected to the more conventional attrition milling. The XRD analyzes, including detailed Rietveld refinements, showed that the captured oxygen does not form solid-solutions but amorphous oxides. The density measurement by helium pycnometry confirmed the formation of such oxides, and was entirely consistent with the phase composition determined by IGF and XRD. The XPS analyzes indicated that these amorphous oxides are ZrO_2 and B_2O_3, something that could not be determined by the FTIR or Raman spectroscopy, and that they locate preferentially on the surface of the powder particles, in perfect agreement with the direct TEM observations.

[1] Taking an average agglomerate size of 200 nm and a primary particle size of 10 nm with the assumption of spherical agglomerates, the inter-particle boundary area per unit volume within each agglomerate is $1.67 \times 10^7\ m^{-1}$.

Acknowledgement

This work was supported by the Ministerio de Ciencia y Tecnología (Government of Spain) under Grant N° MAT 2007-61609.

References

[1] A.L. Chamberlain, W.G. Fahrenholtz, G.E. Hilmas, Pressureless sintering of zirconium diboride, J. Am. Ceram. Soc. 89 (2) (2006) 450–456.
[2] S.C. Zhang, G.E. Hilmas, W.G. Fahrenholtz, Pressureless densification of zirconium diboride with boron carbide additions, J. Am. Ceram. Soc. 89 (5) (2006) 1544–1550.
[3] W.G. Fahrenholtz, G.E. Hilmas, I.G. Talmy, J.A. Zaykoski, Refractory diborides of zirconium and hafnium, J. Am. Ceram. Soc. 90 (5) (2007) 1347–1364.
[4] S.-Q. Guo, Densification of ZrB_2-based composites and their mechanical and physical properties: a review, J. Eur. Ceram. Soc. 29 (6) (2009) 995–1011.
[5] S. Zhu, W.G. Fahrenholtz, G.E. Hilmas, S. Zhang, Pressureless sintering of zirconium diboride using boron carbide and carbon additions, J. Am. Ceram. Soc. 90 (11) (2007) 3660–3663.
[6] W.G. Fahrenholtz, G.E. Hilmas, S.C. Zhang, S. Zhu, Pressureless sintering of zirconium diboride: particle size and additive effects, J. Am. Ceram. Soc. 91 (5) (2008) 1398–1404.
[7] M. Thompson, W.G. Fahrenholtz, G. Hilmas, Effect of starting particle size and oxygen content on densification of ZrB_2, J. Am. Ceram. Soc. 94 (2) (2011) 429–435.
[8] C. Herring, Effect of change of scale on sintering phenomena, J. Appl. Phys. 21 (4) (1950) 301–303.
[9] R. Telle, L.S. Sigl, K. Takagi, Boride-based hard materials, in: R. Riedel (Ed.), Handbook of Ceramic Hard Materials, vol. 2, Wiley-VCH, Weinheim, 2000, pp. 802–945.
[10] S.L. Dole, S. Prochazka, R.H. Doremus, Microstructural coarsening during sintering of boron carbide, J. Am. Ceram. Soc. 72 (6) (1989) 958–966.
[11] S. Zhu, W.G. Fahrenholtz, G.E. Hilmas, S.C. Zhang, Pressureless sintering of carbon-coated zirconium diboride powders, Mater. Sci. Eng. A 459 (1–2) (2007) 167–171.
[12] H. Zhang, Y. Yan, Z. Huang, X. Liu, D. Jiang, Pressureless sintering of ZrB_2–SiC ceramics: the effect of B_4C content, Scripta Mater. 60 (7) (2009) 559–562.
[13] S.C. Zhang, G.E. Hilmas, W.G. Fahrenholtz, Mechanical properties of sintered ZrB_2–SiC ceramics, J. Eur. Ceram. Soc. 31 (5) (2011) 893–901.
[14] X.-G. Wang, W.-M. Guo, G.-J. Zhang, Pressureless sintering mechanism and microstructure of ZrB_2–SiC ceramics doped with boron, Scripta Mater. 61 (2) (2009) 177–180.
[15] C.A. Galán, A.L. Ortiz, F. Guiberteau, L.L. Shaw, Crystallite size refinement of ZrB_2 by high-energy ball milling, J. Am. Ceram. Soc. 92 (12) (2009) 3114–3117.
[16] C.A. Galán, A.L. Ortiz, F. Guiberteau, L.L. Shaw, High-energy ball milling of ZrB_2 in the presence of graphite, J. Am. Ceram. Soc. 93 (10) (2010) 3072–3075.
[17] V. Zamora, A.L. Ortiz, F. Guiberteau, M. Nygren, L.L. Shaw, On the crystallite size refinement of ZrB_2 by high-energy ball-milling in the presence of SiC, J. Eur. Ceram. Soc. 31 (13) (2011) 2407–2414.

[18] B.R. Lawn, Fracture of Brittle Solids, Cambridge, UK, Cambridge University Press, 1993.
[19] C. Suryanarayana, Mechanical alloying and milling, Prog. Mater. Sci. 46 (1–2) (2001) 1–184.
[20] P.R. Soni, Mechanical Alloying. Fundamental and Applications, Cambridge International Science Publishing, Cambridge, UK, 2001.
[21] V. Zamora, A.L. Ortiz, F. Guiberteau, M. Nygren, Crystal-size dependence of the spark-plasma-sintering kinetics of ZrB_2 ultra-high-temperature ceramics, J. Eur. Ceram. Soc. 32 (2) (2012) 271–276.
[22] J. Watts, G. Hilmas, W.G. Fahrenholtz, D. Brown, B. Clausen, Measurement of thermal residual stresses in ZrB_2–SiC composites, J. Eur. Ceram. Soc. 31 (9) (2011) 1811–1820.
[23] L. Huerta, A. Durán, R. Falconi, M. Flores, R. Escamilla, Comparative study of the core level photoemission of the ZrB_2 and ZrB_{12}, Physica C 470 (9–10) (2010) 456–460.
[24] D. Alfano, L. Scatteia, F. Monteverde, E. Bêche, M. Balat-Pichelin, Microstructural characterization of ZrB_2–SiC based UHTC tested in the MESOX plasma facility, J. Eur. Ceram. Soc. 30 (11) (2010) 2345–2355.